RESEARCH ARTICLE

Turbulent near wake of an Ahmed vehicle model

X. W. Wang · Y. Zhou · Y. F. Pin · T. L. Chan

Abstract The lasting high fuel cost has recently inspired resurgence in drag reduction research for vehicles, which calls for a thorough understanding of the vehicle wake. The simplified Ahmed vehicle model is characterized by controllable flow separation, thus especially suitable for this purpose. In spite of a considerable number of previous investigations, our knowledge of flow around this model remains incomplete. This work aims to revisit turbulent flow structure behind this model. Two rear slant angles, i.e., $\alpha = 25°$ and $35°$, of the model were examined, representing two distinct flow regimes. The Reynolds number was 5.26×10^4 based on the model height (H) and incident flow velocity. Using particle image velocimetry (PIV), flow was measured with and without a gap ($g/H = 0.174$) between the vehicle underside and ground in three orthogonal planes, viz. the x–z, x–y and y–z planes, where x, y, and z are the coordinates along longitudinal, transverse, and spanwise directions, respectively. The flow at $g/H = 0$ serves as an important reference for the understanding of the highly complicated vehicle wake ($g/H \neq 0$). While reconfirming the well-documented major characteristics of the mean flow structure, both instantaneous and time-averaged PIV data unveil a number of important features of the flow structure, which have not been previously reported. As such, considerably modified flow structure models are proposed for both regimes. The time-averaged velocities, second moments of fluctuating velocities, and vorticity components are presented and discussed, along with their dependence on g/H in the two distinct flow regimes.

X. W. Wang · Y. Zhou (✉) · Y. F. Pin · T. L. Chan
Department of Mechanical Engineering, The Hong Kong
Polytechnic University, Hung Hom, Kowloon, Hong Kong
e-mail: mmyzhou@polyu.edu.hk

1 Introduction

The global warming and lasting high fuel costs in the past few years highlight the necessity and urgency of drag reduction research for vehicles, which warrants a thorough understanding of flow around vehicles because of a connection between the flow structure and aerodynamic drag. Past studies have unveiled that the pressure drag contributes predominantly to the total drag acting on vehicles, in particular at a high speed. The pressure drag is generated largely by the after-body for most cars, with little contribution from the fore-body (Hucho and Sovran 1993), and is directly linked to the coherent structures in the vehicle wake (Beaudoin and Aider 2008). As such, the wake of three-dimensional (3-D) vehicle models has caught considerable attention in the past because of its fundamental and engineering significance (Oertel 1990); a large number of experimental and numerical investigations have been performed since the pioneer work of Janssen and Hucho (1974).

The so-called Ahmed body (Ahmed et al. 1984) is perhaps the most widely studied simplified car model, which is a 3-D bluff body. Its blunt fore-body is designed to avoid separation so that the aerodynamic forces depend largely on the flow structure created on its after-body. This flow structure is unsteady, very complicated, and highly 3-D, including three major components: a recirculation bubble over the rear slanted surface, longitudinal vortices originating from the two side edges or C-pillars of the surface, and a recirculation torus in the base of the model. The strength and behaviors of the three types of coherent structures and their interactions depend on the slant angle (α) of the upper rear surface of the model (Ahmed et al. 1984). Please refer to Fig. 1 for the schematic of the coherent structures for $\alpha \leq 30°$ and Fig. 2 for the
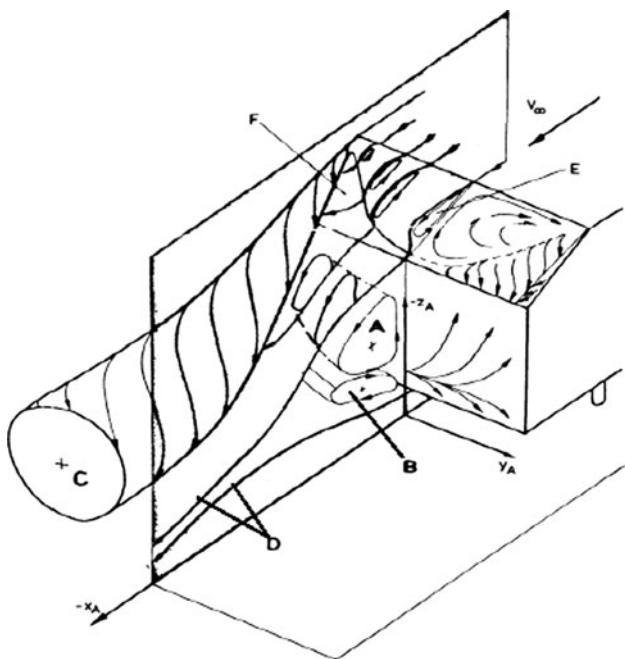
Fig. 1 Schematic of the flow structure behind a 3-D Ahmed vehicle model (from Ahmed et al. 1984): $\alpha = 30°$, the high drag flow. The flow structure is characterized by recirculatory bubbles "A" and "B" inside separation bubble "D", longitudinal vortex "C" formed from the side edge of the rear window, half elliptic region of circulatory "E" and flanked by 2 triangular attached flow region "F" on the slant surface
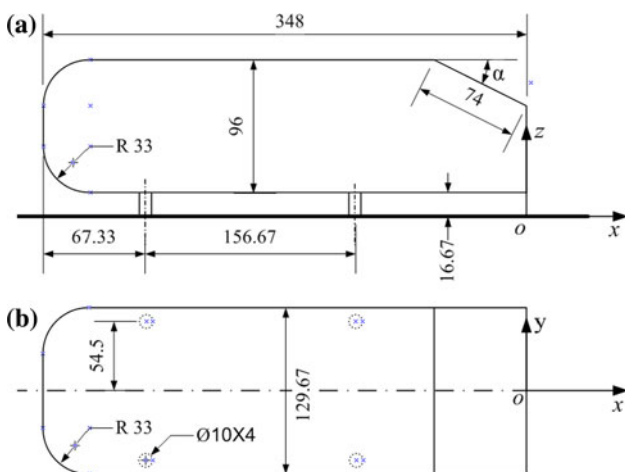

Fig. 2 Dimensions of the scaled-down Ahmed vehicle model and the definition of the coordinate system: **a** side view, **b** plan view. The length unit is mm and angle is in degree

reduction. The minimum drag occurs at $\alpha = 12.5°$. The flow at this α appears to be "two-dimensional" (2-D) except in the vicinity of the two C-pillars of the surface. This is evident from the parallel isobars of static pressure running across the surface (Ahmed et al. 1984). Beyond $\alpha \approx 15°$, the flow over the rear slanted surface becomes highly 3-D. The pressure drag rises rapidly with increasing α and reaches the maximum at $\alpha = 30°$, where the two longitudinal vortices achieve their maximum strength. At $\alpha > 30°$, the flow is dominated by spanwise vortices with the longitudinal vortices burst, and the pressure drag falls despite a fully separated flow. Apparently, $\alpha = 30°$ is a division point for two distinct regimes (Hucho and Sovran 1993). The flow is highly sensitive to a small change in α at the critical configuration. This is evident in Sims-Williams's (2001) detailed study of the time-averaged and unsteady flow structures at $\alpha = 30°$ based on 5-hole probe and smoke flow visualization measurements.

Previous studies have greatly advanced our understanding of the flow structure behind the Ahmed model and meanwhile raised a number of issues to be resolved or clarified. For example, flow structure models were proposed, which are different from the well-known model shown in Ahmed et al. (1984). Vino et al. (2005) investigated experimentally flow structures in the near wake of the Ahmed model ($\alpha = 30°$) using a 13-hole probe, which allowed reliable measurements in regions exhibiting large flow angles, including flow reversals. Their time-averaged results showed good agreement with previously published data at x/H = 1.09 but not at 0.044, much of inconsistency being connected to interactions between the separated flow over the slant and the recirculatory flow in the vertical base of the vehicle model. Their detached flow over the slant was not fully reattached, in deviation from what Ahmed et al. (1984) suggested; that is, the flow above the central region of the slant (Fig. 1) was reattached, forming a separation bubble, before separating again from the base. Based on their numerical data, Krajnovic and Davidson (2005b) also questioned the correctness of Ahmed et al.'s (1984) flow structure model and even suggested that the pair of downstream longitudinal vortices did not stem from the shear layer rollup about the side edge of the slanted surface (their Fig 19). It is worth noting that the Ahmed flow structure model (Fig. 1) was a description of flow valid only for the regime of $\alpha = 12.5°–30°$. A well-quoted flow structure model for $\alpha > 30°$ was constructed based on flow visualization and laser-Doppler anemometer (LDA) measurements from Lienhardt et al. (2000), which showed only two longitudinal structures and recirculation flows over the slant and the vertical base (e.g., Martimat et al. 2008), with many details of the flow structure missing.

Our knowledge of the instantaneous and fluctuating flow fields has yet to be improved, in particular, of the higher

definitions of α and the present coordinate system. At small α, the flow is characterized by two counter-rotating longitudinal vortices (e.g., Brunn et al. 2007). The vortices produce drag on one hand and induce a downwash between them, which enhances flow attachment on the slanted surface, on the other hand. The net effect is a drag

order statistical moments of fluctuating velocities such as the Reynolds stresses. This knowledge is important for a thorough understanding and control of vehicle aerodynamics and also crucial for the validation of numerical models. Bearman (1997) measured using PIV the wake of a 1/8 scale fastback vehicle and noted a significant difference between time-averaged and unsteady flow structures behind the model. The instantaneous flow consisted of a substantial number of more compact coherent structures that occurred rather randomly in time and space, while the time-averaged flow was dominated by a pair of counter-rotating longitudinal vortices. Using LDA and hotwire, Lienhart and Becker (2003) measured rather extensively the higher order statistical moments of velocities as well as the mean velocities behind Ahmed vehicle model at $\alpha = 25°$ and $35°$, though with little discussion of flow physics.

The well-known wake structure model for $\alpha < 30°$ is characterized by one pair of counter-rotating longitudinal vortices. However, based on the numerical simulation of the Ahmed vehicle model at $\alpha = 25°$ with $g/H = 0.174$, Krajnovic and Davidson (2005a) pointed to the presence of one more pair of counter-rotating longitudinal vortices near the lower corner of the side surface, though they considered the vortices to be too weak to be of aerodynamic significance. In this paper, g denotes the gap separation between the ground surface and the model underside and H represents the model height. Strachan et al. (2007) measured using LDA time-averaged velocities behind an Ahmed vehicle model of $\alpha = 0°–40°$, which was supported on an overhead aerodynamic strut. They observed at $g/H = 0.174$ a shear layer near the lower side edge of the model, thus also inferring the presence of one pair of counter-rotating longitudinal vortices, which were referred to as "lower vortices" to be distinguished from the C-pillar vortices. This pair of lower vortices was not reported previously, for example, by Ahmed et al. (1984), Sims-Williams and Duncan (2003), and Vino et al. (2005), who used a 10-hole, a 5-hole, and a 13-hole directional probe, respectively, nor by Lienhart and Becker (2003), who also used an LDA technique. Strachan et al. (2007) ascribed this discrepancy to the use of cylindrical struts used in the earlier investigations and suggested that the struts suppress the formation of the lower vortices. This has been demonstrated to be incorrect in the present investigation. The mechanism behind the lower vortex generation and the dynamic role of this vortex need to be clarified.

One may wonder whether the discrepancy mentioned above has anything to do with g/H ($\neq 0$) due to the presence of wheels. Krajnovic and Davidson (2005b) observed flow separation at the leading lower edge of the vehicle model with $g/H = 0.174$, but not in their earlier studies of a similar vehicle model with $g/H = 0.08$ (Krajnovic and

Davidson 2002, 2003). They subsequently linked the different observations to the clearance effect. So far, this effect on the vehicle aerodynamics has not been given adequate attention in the literature. Note that the wake of the Ahmed model is highly complicated, including three-dimensional and gap effects. By comparing the flow structures with and without an underbody gap, one may identify the part of the flow structure that is generated due to the presence of the gap, thus facilitating the data interpretation.

With the above issues identified in mind, the first objective of this work is to gain through measurements a better picture of the flow structure around the Ahmed vehicle model; the second is to investigate the effect of the clearance between the model underside and the ground surface on the flow structure; the third is to provide the experimental data of the second-order moments of fluctuating velocities as well as the mean velocity field for numerical modeling. Two configurations, i.e., $\alpha = 25°$ and $35°$, were investigated, corresponding to the two distinct flow regimes (Ahmed et al. 1984; Hucho and Sovran 1993). In view of a highly 3-D flow, the PIV measurements were conducted in three orthogonal planes behind the model with and without a clearance between the model underside and the wind tunnel wall. Based on the data obtained, the instantaneous and time-averaged flow fields are examined and discussed, along with the Reynolds stresses and also published results, including modified conceptual flow structure models.

2 Experimental details

2.1 Wind tunnel and vehicle model

Experiments were carried out in a closed circuit wind tunnel with a 2.4-m-long square test section (0.6 m × 0.6 m). The flow non-uniformity in the test section is 0.1 % and the streamwise turbulence intensity is less than 0.4 % in the absence of the vehicle model for the velocity range examined presently. The working section wall was made of optical glass in order to enhance the signal-to-noise ratio in PIV measurements. See Huang et al. (2006) for more details of the tunnel. The dimensions of a 1/3-scaled Ahmed vehicle model are given in Fig. 2. Two angles, i.e., $\alpha = 25°$ and $35°$, were investigated. The model is 0.348 m in length (L), 0.13 m in width (B), and 0.096 m in H, placed on a flat plate (length x width x thickness = 2 m × 0.59 m × 0.02 m) raised from the floor of the working section. The four wheels of the model were simulated by four 16.67-mm-tall struts with a diameter of 10 mm. The front end of the model was 0.3 m downstream of the leading edge of the plate. The blockage

ratio of the frontal surface of the model to the rectangular test section above the flat plate was around 4.1 %, not exceeding 5 %, a suggested limit beyond which the blockage effect cannot be neglected (Farell et al. 1977). The leading edge of the plate was a clipper-built curve, following Narasimha and Prasad's (1994) design, to avoid flow separation. Measurements were conducted at the free-stream velocity $U_\infty = 8.33$ m/s, corresponding to a Reynolds number, $Re_H \equiv U_\infty H/v = 0.53 \times 10^5$, where v is the kinematic viscosity of air. The Re_H effect on the flow will not be investigated in this paper, though not systematically documented in the literature. While the design of the Ahmed model aimed to minimize flow separation from its fore-body and to have fixed flow separation from its after-body owing to the clearly defined corners, Minguez et al.'s (2008) large eddy simulation at $Re_H = 7.68 \times 10^5$ showed that flow separated at the fore-body and then reattached on the roof and lateral sides, forming a bubble, which suggests a dependence of the flow structure on Re_H. Limited drag coefficient and Strouhal number data also show a variation, albeit slightly, with increasing Re_H (e.g., Vino et al. 2005; Joseph et al. 2011; Thacker et al. 2012).

The coordinate system (Fig. 2) follows the right-hand rule and is defined such that x, y, and z are directed along the mean flow, vertical (transverse), and spanwise directions, respectively. In this paper, asterisk denotes normalization by H and/or U_∞, e.g., $x^* = x/H$, $y^* = y/H$ and $z^* = z/H$. The instantaneous velocity components in the x, y, and z directions are designated as U, V, and W, respectively. An instantaneous velocity may be decomposed into an averaged component and a fluctuating component, viz. $U = \overline{U} + u'$, $V = \overline{V} + v'$, $W = \overline{W} + w'$, where overbar denotes time-averaging, and u', v', and w' are the fluctuating velocity components, out of which the root mean square values, u_{rms}, v_{rms}, and w_{rms}, may be calculated.

2.2 Documentation of boundary layer

The boundary layer over the plate may have an effect on the flow structure around a finite-height bluff body (Wang et al. 2006). It is therefore important to document the conditions of the boundary layer, where the model was placed. An LDA system (Dantec Model 58N40) with an enhanced flow velocity analyzer was used to measure $\overline{U}$ and u_{rms} at 0.3 m from the leading edge of the plate in the plane of symmetry. The flow was seeded by smoke generated from paraffin oil with an averaged particle size of around 1 μm in diameter. The measuring volume of the LDA system had a major axis of 2.48 mm and a minor axis of 1.18 mm. More than 5,000 instantaneous samples were collected at each point. The boundary layer disturbance thickness, estimated based on $\overline{U}$, was about 4 mm (i.e.,

0.036H), estimated from the $\overline{U}$ distribution. Such a thin boundary layer should produce a negligibly small effect on the flow structure.

2.3 PIV measurements

A DANTEC standard PIV system was used to measure flow around the Ahmed model with and without the four struts (wheels), i.e., $g^* = 0.174$ and 0, in order to understand the effect of the clearance between the model underside and wall on the flow structure. The schematic of experimental setup is shown in Fig. 3. The same seeding was used as in the LDA measurement. Flow illumination was provided by two New wave standard pulsed laser sources of 532 nm wavelength, each with a maximum energy output of 120 mJ/pulse. Each laser pulse lasted for 0.01 μs. Particle images were taken using a CCD camera (HiSense type 4 M, double frames, 2,048 × 2,048 pixels). Synchronization between image taking and flow illumination was provided by the Dantec FlowMap processor (System HUB).

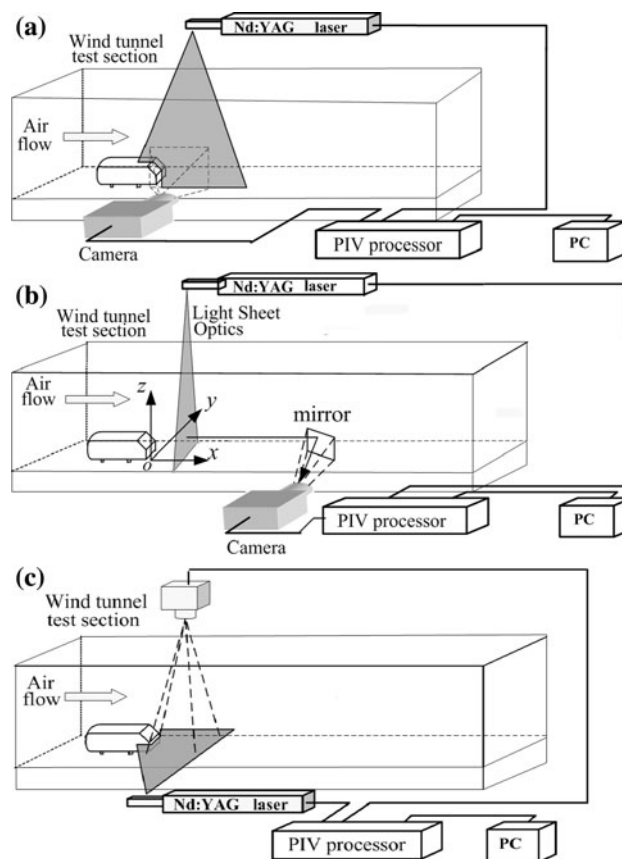The flow is highly three-dimensional (Ahmed et al. 1984). In order to capture accurately the flow structure, one

Fig. 3 PIV measurement arrangements in **a** the x–z plane, **b** y–z plane, and **c** x–y plane

should ideally conduct measurements around the model in a large number of planes along each of the x, y, and z directions. This is unpractical because of the demands for a tremendously large storage space of data and also an exhaustive amount of time and effort for data analysis. Therefore, PIV measurements were performed in a limited number of planes, including the x–z plane at $y^* = 0$ (symmetry plane), the x–y plane at mid-height of the model from wall, i.e., $z^* = 0.59$ at $g^* = 0.174$ or $z^* = 0.5$ at $g^* = 0$, and the y–z plane at $x^* = 0.23$ and 5.00, one in the near wake and the other in the far wake, i.e., within and outside the recirculation region, respectively. Different measurement planes are illustrated in Fig. 3. For the measurements in the y–z plane, a mirror of 120 mm × 120 mm was vertically placed at $x/H = 15$ in the tunnel, whose normal direction was 135° from the x-axis. At such a distance downstream of the PIV imaging plane, the camera should have a negligibly small effect on the measurement (Zhang et al. 2006). The PIV images covered an area of 2.4H × 2.4H ($x^* = -0.6$–1.8, $z^* = -0.15$–2.25), 2.4H × 2.4H ($y^* = -1.2$–1.2, $z^* = -0.2$–2.2), and 1.96H × 1.96H ($x^* = -0.06$–1.9, $y^* = -0.98$–0.98) for the x–z, y–z, and x–y planes, respectively. The image magnifications in both directions of the plane were identical, ranging from 103 to 113 μm/pixel. The interval between two successive pulses was set at 50 μs for measurements in the x–y and x–z planes, during which fluid particles may travel a distance of 0.42 mm at $U_\infty = 8.33$ m/s. Following Huang et al. (2006), the laser sheet was made thicker for measurements in the y–z plane, i.e., 3 mm (cf. 1.0–1.5 mm in the x–y and x–z planes) in order to capture the maximum number of seeding particles during each pulse.

In processing PIV images, 32 × 32 interrogation areas were used with a 50 % overlap in each direction, producing 127 × 127 in-plane velocity vectors and the same number of vorticity components $\Omega_x = \overline{\Omega_x} + \omega_x$, $\Omega_y = \overline{\Omega_y} + \omega_y$, or $\Omega_z = \overline{\Omega_z} + \omega_z$ in the x, y, and z directions, respectively, where ω_x, ω_y, and ω_z are the fluctuating vorticity components, respectively. The vorticity data were calculated by a built-in function of the FlowMap Processor based on eight surrounding velocity data. The spatial resolution of vorticity data was about 1.81 mm, 1.81 mm, and 1.66 mm for the x–z, y–z, and x–y planes, respectively.

A total of 1,100 PIV images were captured in each plane. The number of images needs to be adequate for determining both mean and fluctuating flow fields. The dependence of $\delta = \frac{\beta_N - \beta_{N-\Delta N}}{\beta_N}$ on N was calculated, where β denotes $\overline{U}^*$, $\overline{W}^*$, u_{rms}^* or w_{rms}^*, and $\overline{\Omega_y}$, and subscript N or $N-\Delta N$ is the number of images (ΔN is the increment in N). The velocity data were obtained with $g^* = 0.174$ at (x^*, y^*, z^*) = 0.23, 0, 0.4 in the x–z plane. The parameter δ

provides a measure of the dependence of experimental uncertainties on N and converges rapidly, with increasing N, to less than ±1 % at N ≈ 800 at $\alpha = 25°$ or 35° for all the quantities (not shown). Similar results have been obtained at other locations, thus demonstrating that 1,100 images are adequate presently.

3 Longitudinal structures

3.1 Time-averaged flow

The wake of the Ahmed vehicle model is characterized by predominantly longitudinal structures that play a crucial role in determining aerodynamic forces (e.g., Ahmed et al. 1984). Naturally, the longitudinal structures have been a focus in previous experimental investigations, most of which were performed based on time-averaged data perhaps due to a limitation in measurement techniques. As such, time-averaged data are presently examined first to facilitate data comparison and interpretation. Figure 4 compares the iso-contours of $\overline{\Omega_x^*}$ in the y–z plane at $x^* = 0.23$ with and without a gap of $g^* = 0.174$ for $\alpha = 25°$ and 35°. The same cutoff contour level and increment are used in the four plots of Fig. 5 and those following to facilitate comparison. The flow structure appears highly complicated, displaying many vorticity concentrations, as noted by Bearman (1997). A close inspection of the contours unveils interesting details on the flow structure, as well as the major flow characteristics that conform to previous numerical and experimental studies (Ahmed et al. 1984; Lienhart et al. 2003; Sims-Williams et al. 2001; Krajnovic and Davidson 2005a; Vino et al. 2005; Minguez et al. 2009).

At $\alpha = 25°$ (Fig. 4a), a number of observations can be made. Firstly, the two most concentrated longitudinal vortices, marked by "C", are well-known C-pillar vortices. Their centers are located at (y^*, z^*) ≈ (-0.56, 0.9) and (0.52, 0.9), respectively. With flow blowing over the vehicle body, the shear layers over the C-pillars roll up into the longitudinal or C-pillar vortices. Secondly, there are many vorticity concentrations behind the model vertical base, which tend to be aligned in two rows, one at the same level of the upper edge of the base and the other right above the lower edge. These structures probably result from the shear layer separation from the upper and lower edges, that is, they are associated with the two recirculatory bubbles, one above the other, and referred to as vortices "A" and "B" by Ahmed et al. (1984) see Fig. 1. The signs of the structures near the upper edge tend to occur alternately, which have not been reported previously and will be discussed later in detail together with instantaneous
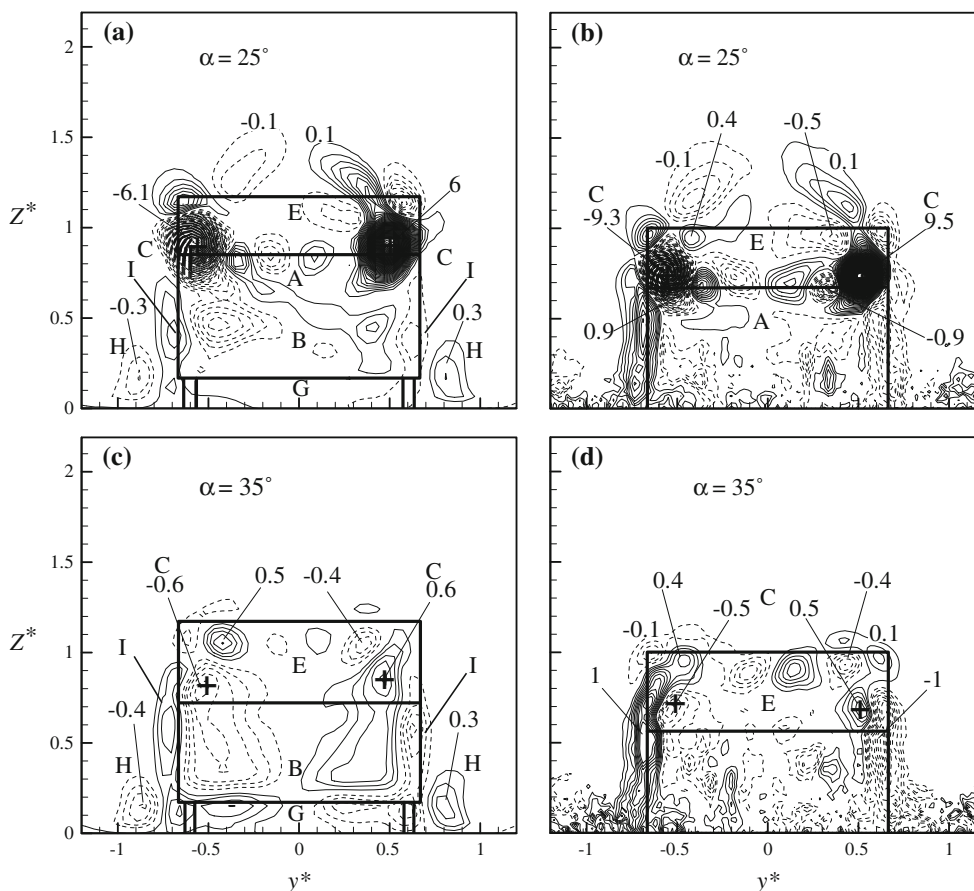
Fig. 4 Iso-contours of averaged streamwise component, $\overline{\Omega_x}^*$, of vorticity in the y–z plane at $x^* = 0.23$ ($Re_H = 5.26 \times 10^4$): **a**, **c** $g^* = 0.174$, **b**, **d** $g^* = 0$. The contour interval is 0.1 and the cutoff level is ± 0.1

vorticity contours. Thirdly, the central region "E" of the slant surface is not associated with large vorticity concentrations. This should be reasonable. Compared with the case of $\alpha < 12.5°$ where flow over the slant surface is rather 2-D and fully attached to the surface (Ahmed et al. 1984), the two longitudinal vortices for $12.5° < \alpha \leq 30°$ grow in size, resulting in a 3-D flow over the slant surface and meanwhile maintaining attached flow over a section of the surface (e.g., Strachan et al. 2007), though the flow separates from and reattaches on the slant surface, forming a separation bubble, when α is close to 30°. Fourthly, a number of concentrations show up above the C-pillar vortices. As will be seen later from the data in the x–z plane, the shear layer developed over the top surface of the model does not entirely remain attached to the slant; rather, part of it shoots over, deviating only slightly from the horizontal direction. The detached shear layer, under the rolling effect of C-pillar vortices, is probably responsible for the concentrations. Fifthly, Fig. 4a displays one additional pair of counter-rotating longitudinal vortices, marked by "H", which occur near the lower corners of the model, one at $(y^*, z^*) \approx (-0.88, 0.16)$ and the other at

$(y^*, z^*) \approx (0.80, 0.16)$. Their maximum vorticity concentration is about 5 % of the C-pillar vortex. Most previous measurements using multi-hole probes, hotwires, or LDA failed to capture the two vortices. The first observation was made by Krajnovic and Davidson (2005a) based on their LES data at $\alpha = 25°$, who considered the vortices to be too weak to be of any aerodynamic significance. Stranchen et al. (2007) made a similar observation based on their LDA data. With their model supported by a single overhead strut, they ascribed the generation of the vortices to four cylindrical struts used in many earlier measurements. A different opinion is offered here. The presence of the boundary layers formed on the wall and the model underside decelerates fluid and hence increases the pressure of the gap flow. The iso-contours of $\overline{V^*}$ in the y–z plane (not shown) indicate a flow squeezed out of the gap, that is, the pressure difference between flow inside the gap and that outside induces the rollup of fluid, forming longitudinal vortices in a manner similar to the C-pillar vortices. The vortices are presently referred to as the lower vortices, following Stranchen et al. (2007). The lower vortices are predominantly longitudinal. As a matter of
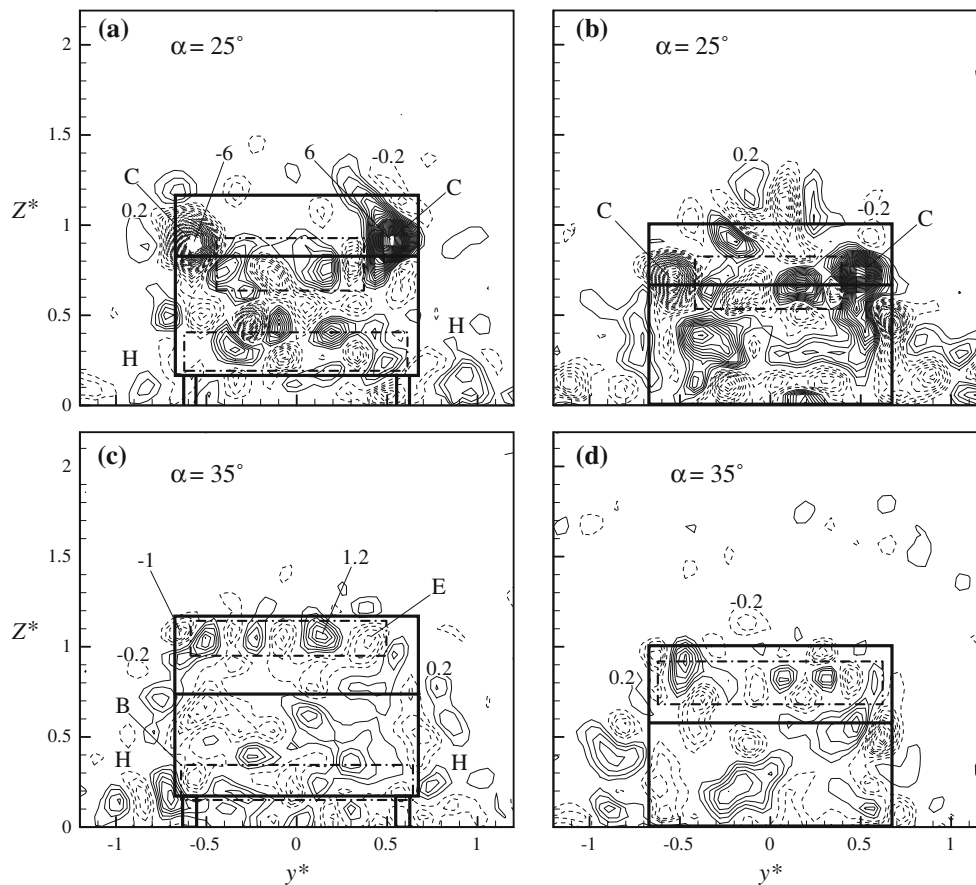
Fig. 5 Iso-contours of instantaneous streamwise component, Ω_x^*, of vorticity in the y–z plane at $x^* = 0.23$ ($Re_H = 5.26 \times 10^4$): **a**, **c** $g^* = 0.174$, **b**, **d** $g^* = 0$. The contour interval is 0.2 and the cutoff level is ± 0.2

fact, supplementary PIV measurements (not shown), conducted in the x–z plane at $y^* = -0.57$ and -0.77, failed to capture any appreciable vorticity concentration at the position where the lower vortices occur. Finally, there is one stretched vorticity concentration, marked by "I", along each side surface of the model, which originates probably from the shear layer developed over the side surface of the model.

In the absence of the gap, i.e., $g^* = 0$ (Fig. 4b), there is a marked change in the flow structure. The most noticeable is perhaps the absence of the lower vortices "H", corroborating our proposition on their generation mechanism. The maximum vorticity concentrations of the C-pillar vortices "C" are increased by about 50 %, though the vortex size shrinks. The vorticity concentrations generated by flow separation from the upper edge of the base, associated with recirculatory bubble "A", are evident and again occur alternately in sign. On the other hand, the lower row of concentrations could not be seen. This is reasonable since the recirculatory bubble "B" results largely from the shear layer separating from the lower edge of the vertical base and upwash flow (Ahmed et al. 1984; Sims-Williams and

Duncan 2003; Vino et al. 2005). Finally, the stretched concentrations "I" are enhanced in both size and the maximum vorticity. The changes suggest that the gap has a profound influence on the wake and hence aerodynamics of ground vehicles.

At $\alpha = 35°$, flow separates from the upper edge of the rear slant surface, and the C-pillar vortices burst (Ahmed et al. 1984). This is reflected in Fig. 4c. Firstly, there is one row of vorticity concentrations, again alternately arranged in sign, right below the upper edge of the slant. They result from flow separation and are brought down by downwash flow. Secondly, the maximum vorticity concentration of vortices "C" diminishes to about 10 % of its counterpart at $\alpha = 25°$ (Fig. 4a). The vortices further exhibit a significant reduction in size, though appearing enlarged due to their merging with vorticity concentrations in the base. The observation is consistent with Ahmed et al.'s (1984) report that the separation region or half elliptic recirculation flow on the slant surface joined the separation bubble of the base so that bubbles "A" and "E" could no longer be considered to be separate. Note that the maximum concentration of the lower vortex "H" retains its strength at $\alpha = 25°$ and

now amounts to about 50 % of the C-pillar vortex. Naturally, its dynamic role may not be necessarily negligible. There is one pair of vortices "G" between the wall and the model underside, apparently linked to the shear layer developed in the gap and hence called the gap vortices. The gap vortex could not be seen in Fig. 4a. As will be shown later, the downwash flow is markedly stronger at $\alpha = 25°$ than at $\alpha = 35°$, thus keeping the gap vortices down, without being captured at the present imaging plane.

In the absence of the gap (Fig. 4d, $\alpha = 35°$), the row of alternately signed vorticity concentrations, resulting from shear layer separation from the upper edge of the slant surface, appears enhanced in strength, albeit slightly. The concentrations "I" are also strengthened. On the other hand, the C-pillar vortex is further impaired in both the maximum vorticity and size, compared to Fig. 4c. So are the concentrations associated with the separation bubble in the model vertical base.

3.2 Instantaneous flow

Most of previous investigations are focused on time-averaged flow field around Ahmed vehicle model for various reasons. Many important details of the flow field could be lost or buried in the time-averaging process. There have been efforts in performing oil or smoke flow visualization to complement the data of time-averaged flow field (e.g., Ahmed et al. 1984; Lienhart and Becker 2003; Vino et al. 2005). These efforts provide flow pictures on the model surface or in the x–z plane and indeed further our understanding of flow physics. The present PIV measurements in three orthogonal planes provide us with a great opportunity to explore instantaneous flow structures of the vehicle model, in particular, in the y–z plane.

Figure 5 illustrates typical Ω_x^*-contours in the y–z plane at $x^* = 0.23$. Apparently, the instantaneous flow structure is highly complicated; the base region is packed with the vortical motions or vorticity concentrations of various scales. Nevertheless, a close inspection allows us to connect these motions to the time-averaged major features shown in Fig. 4. The C-pillar vortices are easily identified in Fig. 5a and b with the pair of the most highly concentrated counter-rotating large-scale vorticity concentrations. The shape and the strange of the C-pillar vortices are similar. These results demonstrate that the longitudinal structures are spatially very stable. (Thacker et al. 2012) The lower vortices are also discernible in Fig. 5a and c. Note that in the absence of the clearance, the vorticity concentrations (Fig. 5b, d) may occur near the lower corners of the model. However, their signs appear rather random, that is, these concentrations tend to cancel out each other in the averaging process, explaining the absence of the lower vortex in Fig. 4b and d.

It is of interest to note that one row of four alternately signed vorticity concentrations occurs between the C-pillar vortices in Fig. 5a and b, corresponding reasonably well to the concentrations between the C-pillar vortices in Fig. 4a and b. Absence of a negative concentration between the positive C-pillar vortex and the positive concentration at $(y^*, z^*) \approx (0.1, 0.85)$ in Fig. 4a is probably due to cancelation by the random change in the size of the positive C-pillar vortex. The row of alternately signed vorticity concentrations near the lower edge of the base in Fig. 5a is also interesting, which may be associated with the recirculatory bubble "B" in the time-averaged flow field. These structures appear smaller-scaled than those right below the upper edge of the base. At $\alpha = 35°$, flow separates from the upper edge of the slant, not the upper edge of the base[5]. Therefore, the alternately signed structures could not be seen near the upper edge of the base but are evident right below the upper edge of the slant (Fig. 5c, d), though again with relatively small scales. The observations suggest a connection between the alternately signed vortical structures and flow separation from the model. One is naturally tempted to beg the question: why do the structures associated with the recirculatory bubbles "A" and "B" tend to occur alternately in sign, which has been confirmed by many plots of instantaneous Ω_x^*-contours we have inspected?

It has been established that the recirculatory bubbles "A" and "B" result from spanwise shedding from the vertical base (Ahmed et al. 1984). Such spanwise structures should be nominally 2-D in the central section, though highly 3-D near their ends. Vino et al. (2005) measured surface pressure and all three fluctuating components of flow velocity around an Ahmed model at $Re_H = 1.2 \times 10^5$. The spectra of the pressure and velocity signals measured behind the base displayed a pronounced peak at a Strouhal number of about 0.4 based on the square root of model frontal area. This is also confirmed by our hotwire measurements (not shown). The result demonstrates unequivocally the presence of quasi-periodical structures. Furthermore, this peak is by far stronger in the spectra of the streamwise and transverse fluctuating velocities than in the spectrum of the spanwise component, suggesting that the coherent structures were predominantly spanwise oriented. The formation nature of the structures, along with their behaviors, prompts us to connect the structures with the Karman vortex street behind a 2-D bluff body. The latter flow has been extensively studied in the literature, with many aspects of its flow physics unveiled. It is now well known that two major types of vortical structures occur in this flow, i.e., the nominally 2-D spanwise vortices and the predominantly longitudinal rib structures (e.g., Zhou and Antonia 1994; Zhang et al. 2000). Evidently, the

streamwise vorticity concentrations observed in the base (Figs. 4a, 5a) could be a manifestation of the longitudinal rib structures. There is another possibility. Flow visualizations (Wu et al. 1996; Williamson 1996) point to a waviness of the spanwise vortices. This has been confirmed

Fig. 6 Schematic of the separated spanwise roll wrapped with the rib structures: **a** scenario 1, **b** scenario 2

by direct numerical simulation (DNS) data (Thompson et al. 1994; Zhang et al. 1995). The spanwise vortices can be shed in either parallel or oblique modes (Williamson 1996). All of these features, *inter alia*, could be associated with the flow structure separated from the upper and lower edges of the base or the upper edge of the slant. A spanwise vortex roll wrapped with rib structures could explain the structures near the lower edge of the base and the upper edge of the slant. On the other hand, in view of the end effects, especially the induction effect of the two C-pillar vortices, the scenario of wavy spanwise rolls is considered to be more likely for the alternately signed structures of relatively larger scale separated from the upper edge of the base, though the possibility that the induction effect of the two C-pillar vortices enhances the rib structures should not be excluded. We will come to this point again when discussing transverse structures in Sect. 5. On the basis of the present data and previous observations, the schematic representations of the two scenarios are constructed in Fig. 6.
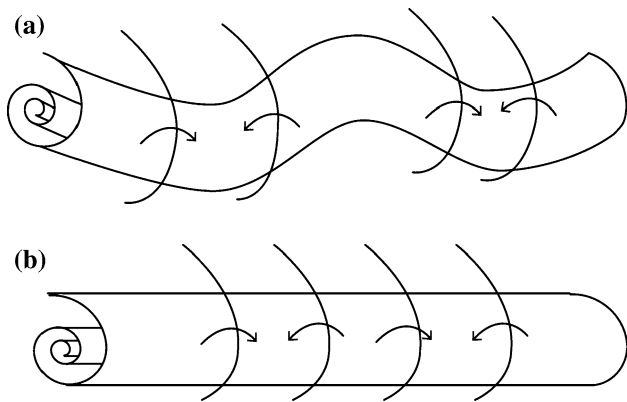
Figure 7 presents the $\overline{W}^*$-contours in the y–z plane at $x^* = 0.23$. The C-pillar vortex centers, identified with the
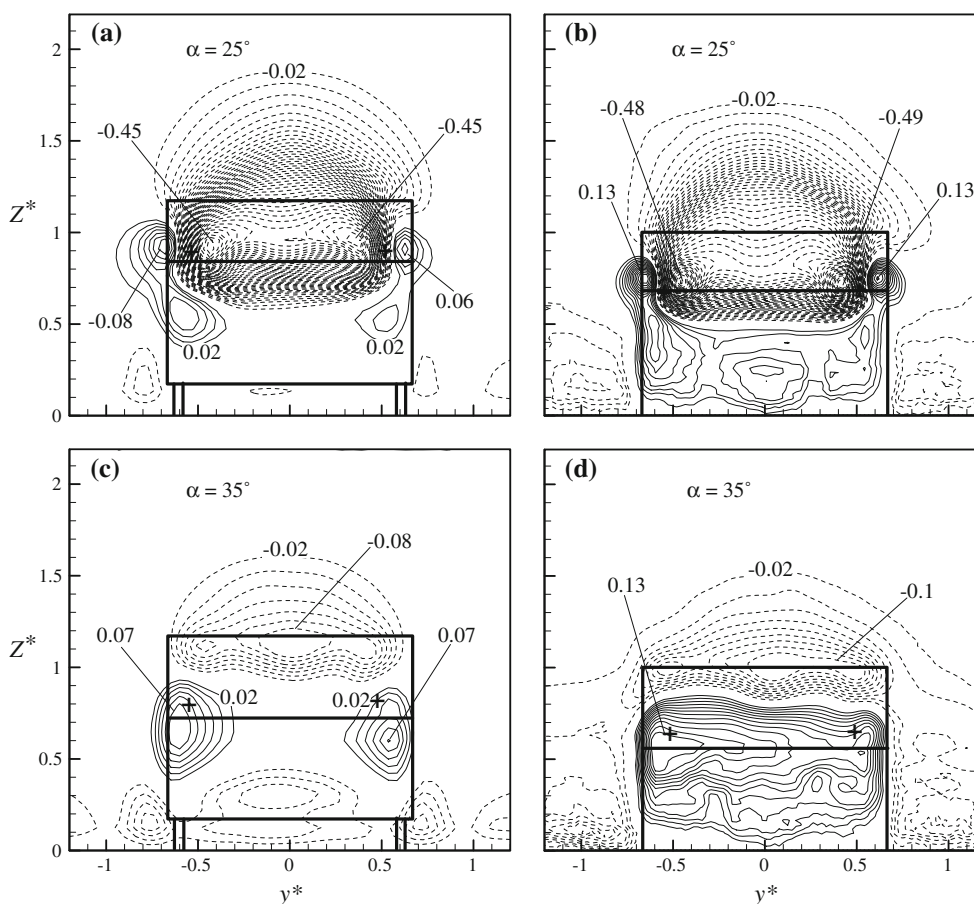

Fig. 7 Iso-contours of the averaged vertical velocity, $\overline{W}^*$, in the y–z plane at $x^* = 0.23$ ($Re_H = 5.26 \times 10^4$): **a**, **c** $g^* = 0.174$, **b**, **d** $g^* = 0$. The contour interval is 0.01 and the cutoff level is ± 0.02

maximum concentrations of the $\overline{\Omega_x^*}$-contours (Fig. 5), have been marked by a cross in Figs. 7, 8, 9, 10, 11 to facilitate interpretation. At $\alpha = 25°$, the negative contours overwhelm over the slant surface, due to the attached downwash flow, and the upper part of the base because of flow separation from the upper edge of the base. The negative contours are flanged by positive concentrations, apparently linked to the C-pillar vortices and the recirculatory bubbles. In the absence of the clearance, the positive concentration is strengthened in the lower base region, due to an upwash flow induced by downwash flow within the recirculation bubble; on the other hand, the negative concentration is enhanced on both sides of the model. At $\alpha = 35°$, downwash flow is greatly weakened with a separation bubble formed over the slant surface. The negative contours in the lower part of the vertical base are probably induced by the vortices resulting from merged C-pillar and recirculatory vortices "B". Without the clearance, the positive contours are extended into the lower half of the slant surface.

Figure 8 shows the iso-contours of the Reynolds shear stress $\overline{vw}^*$ in the y–z plane at $x^* = 0.23$. At $\alpha = 25°$, the relatively high level $\overline{vw}^*$ is mostly concentrated within the C-pillar vortices (c.f. Fig. 4a), that is, the C-pillar vortices are largely responsible for the production of $\overline{vw}^*$. The clover-leaf pattern about the vortex center resembles that associated with the spanwise vortex in the near wake of a 2-D bluff body (Zhou and Yiu 2006). The small magnitude of $\overline{vw}^*$ outside the C-pillar vortices is ascribed to the fact that other longitudinal vortices tend to occur rather randomly in location, and hence, the associated positive and negative vw mostly cancel out each other in averaging. In the absence of the clearance, the $\overline{vw}^*$ (Fig. 8b) occurs again mostly within the C-pillar vortices and its maximum magnitude doubles that in Fig. 8a because of the significantly increased maximum vorticity of the C-pillar vortices (Fig. 4a, b). At $\alpha = 35°$, the $\overline{vw}^*$ concentration (Fig. 8c, d) diminishes considerably due to the burst of the C-pillar vortices.

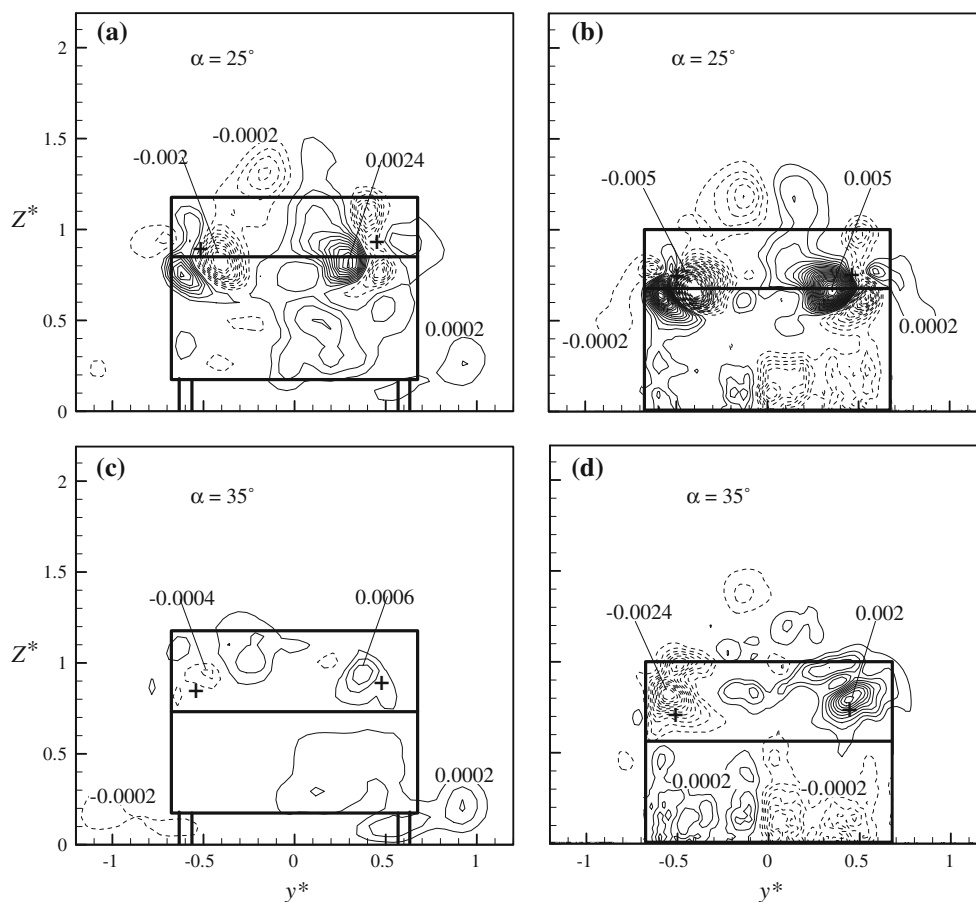**Fig. 8** Iso-contours of the averaged Reynolds shear stress, $\overline{vw}^*$, in the y–z plane at $x^* = 0.23$ ($Re_H = 5.26 \times 10^4$): **a**, **c** $g^* = 0.174$, **b**, **d** $g^* = 0$. The contour interval is 0.0002 and the cutoff level is ± 0.0002
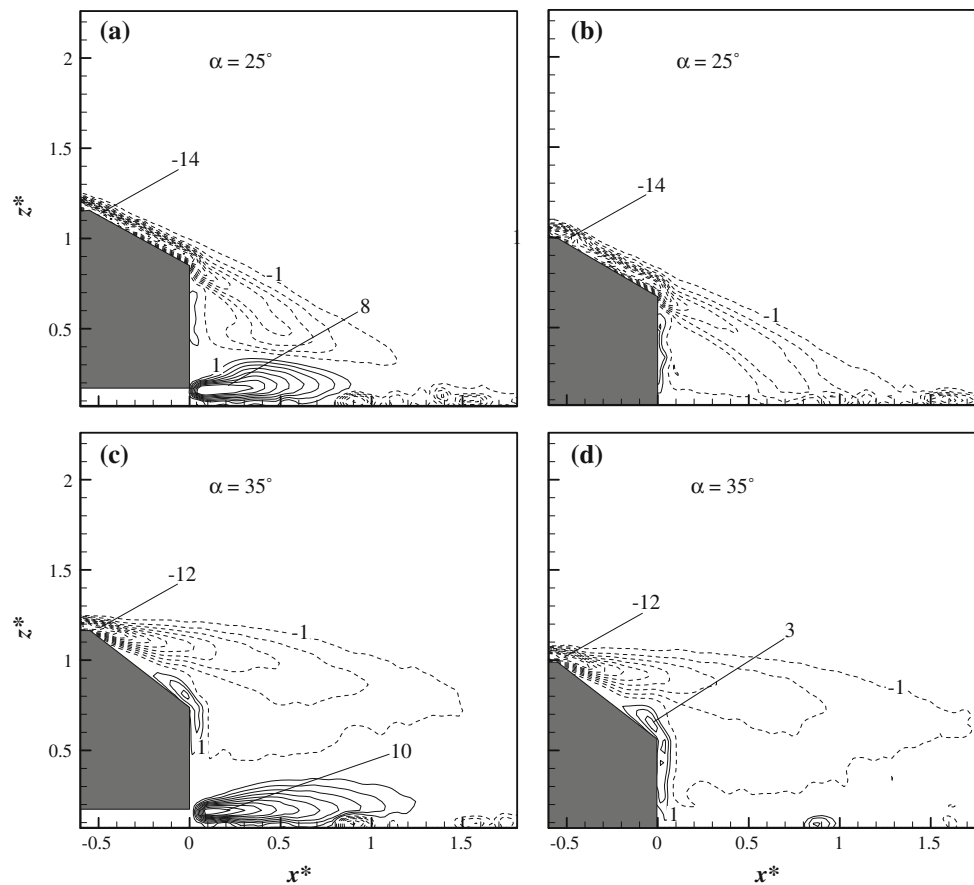
Fig. 9 Iso-contours of the averaged spanwise component of vorticity, $\overline{\Omega_y^*}$, in the x–z plane at $y^* = 0$ ($Re_H = 5.26 \times 10^4$): **a, c** $g^* = 0.174$, **b, d** $g^* = 0$. The contour interval is 1.0 and the cutoff level is ± 1

4 Spanwise structures

The knowledge of spanwise structures is essential for us to understand thoroughly the highly 3-D flow structure around an Ahmed vehicle model. Figure 9 shows the iso-contours of $\overline{\Omega_y^*}$ in the x–z plane at $y^* = 0$. At $\alpha = 25°$, the $\overline{\Omega_y^*}$-contours (Fig. 9a, b) remain attached to the slant surface, be $g^* = 0$ or not. Two recirculatory bubbles are evident at $g^* = 0.174$ (Fig. 9a), which are separated from the upper and lower edges and are referred to in Sect. 3 as vortices "A" and "B", respectively, though bubble "B" disappears at $g^* = 0$ (Fig. 9b). At $\alpha = 35°$, flow separates from the upper edge of the slant, rather than the lower edge (Fig. 9c, d). Naturally, the recirculatory bubble "A" is absent. There is a small region of positive $\overline{\Omega_y^*}$-contours attached to the vertical base at $\alpha = 25°$ or both the slant and vertical base at $\alpha = 35°$, induced by the negative circulation. Recirculatory bubble "B" exhibits a considerably larger strength in terms of the maximum vorticity concentration and size at $\alpha = 35°$ than at $\alpha = 25°$. As shown in Fig. 7, downwash

flow is by far stronger at $\alpha = 25°$ than at $\alpha = 35°$, acting to hold bubble "B" down and to restrain its development. It is worth noting that vortex "A" or "B" produces a much higher vorticity concentration in the x–z plane than in the y–z plane (Fig. 5), suggesting its overwhelmingly spanwise orientation.

Typical instantaneous Ω_y^*-contours are illustrated in Fig. 10, with the major features consistent with the time-averaged data (Fig. 9). For example, at $\alpha = 25°$, there is one highly concentrated negative vorticity layer attached to the slant surface. After separating from the upper edge of the base, part of it rolls up, forming a recirculation behind the base, and the other part appears shooting toward the wall and then breaking up (Fig. 10a) or rebounding downstream (Fig. 10b). There are some vorticity concentrations downstream of the base and above the body. These structures correspond to the concentrations above the top of the model observed in Fig. 4a and b. The upper recirculatory bubble "A" and lower "B" are evident with $g^* = 0.174$; "B" is absent with $g^* = 0$. Flow separation
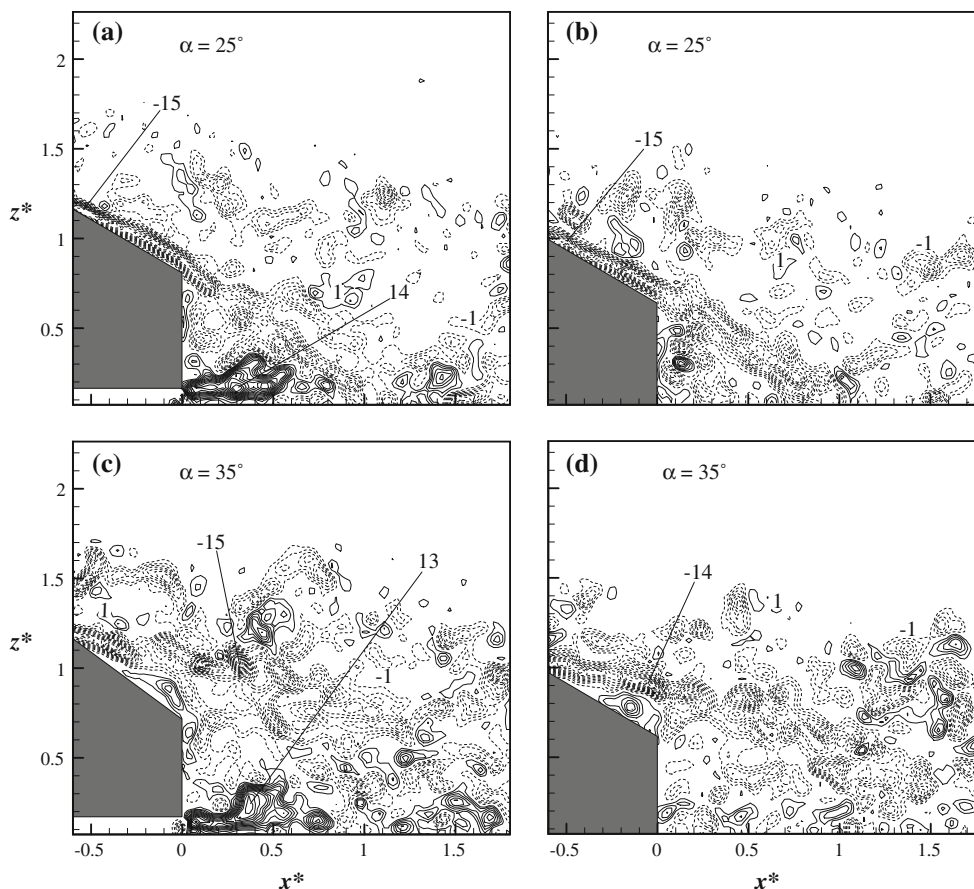
Fig. 10 Iso-contours of the instantaneous spanwise component of vorticity, Ω_y^*, in the x–z plane at $y^* = 0$ ($Re_H = 5.26 \times 10^4$): **a, c** $g^* = 0.174$, **b, d** $g^* = 0$. The contour interval is 1.0 and the cutoff level is ± 1.0

occurs at the upper edge of the slant at $\alpha = 35°$ and bubble "A" is not seen, with the separation bubble over the slant and that behind the base connected (Fig. 10c, d).

The distribution of the mean streamwise velocity, $\overline{U}^*$, in the x–z plane may allow us to determine the extent of the reversed flow region or wake bubble, which may provide us with the information on aerodynamic pressure drag. The reversed flow region is identified with negative $\overline{U}^*$ and is enclosed by $\overline{U}^* = 0$, which is highlighted by a thick solid contour in Fig. 11. Its maximum longitudinal length is defined as the bubble or recirculation length. This length is 0.67H at $\alpha = 25°$ and grows to 1.03H at $\alpha = 35°$ for $g^* = 0.174$. At $\alpha = 35°$, the recirculation region grows significantly, including a small region attached to the slant surface and a region behind the vertical base, as observed by Lienhart and Becker (2003) at the same α and also Vino et al. (2005) at $\alpha = 30°$. The variation of the recirculation length with α is consistent with the difference in the pressure drag coefficient due to the vertical base, which is 0.080 at $\alpha = 25°$ and 0.095 at $\alpha = 35°$ [5]. In the absence of

the clearance ($g^* = 0$), the $\overline{U}^* = 0$ contour does not end on the vertical base but on the wall, without forming a recirculation region, though the longitudinal length of $\overline{U}^* = 0$ is prolonged to 0.86H at $\alpha = 25°$ and 1.43H at $\alpha = 35°$.

The $\overline{W}^*$-contours in the x–z plane at $y^* = 0$ (Fig. 12) essentially conform to the flow structure models proposed by Ahmed et al. (1984). Four concentrations are seen at $\alpha = 25°$ and $g^* = 0.174$ (Fig. 12a). The upper two are connected to the motion of bubble "A" and the lower two are linked to bubble "B", which could not be seen naturally at $g^* = 0$ (Fig. 12b, d). At $\alpha = 35°$, the positive concentration of $\overline{W}^*$ attached to the vertical base is extended to the area over the slant due to flow separation from the upper edge of the slant; the two negative concentrations are merged.

The Reynolds shear stress, $\overline{uw}^*$, in the x–z plane ($y^* = 0$) shows three concentrations at $\alpha = 25°$ and $g^* = 0.174$ (Fig. 13a). The upper and lower concentrations behind the base are connected to bubbles "A" and "B", respectively. The lower is positive and the upper is

Fig. 11 Iso-contours of averaged streamwise velocity, $\overline{U}^*$, in the x–z plane at $y^* = 0$ ($Re_H = 5.26 \times 10^4$): **a**, **c** $g^* = 0.174$, **b**, **d** $g^* = 0$. The contour interval is 0.05. The cutoff levels are $+1.0$ and -0.05
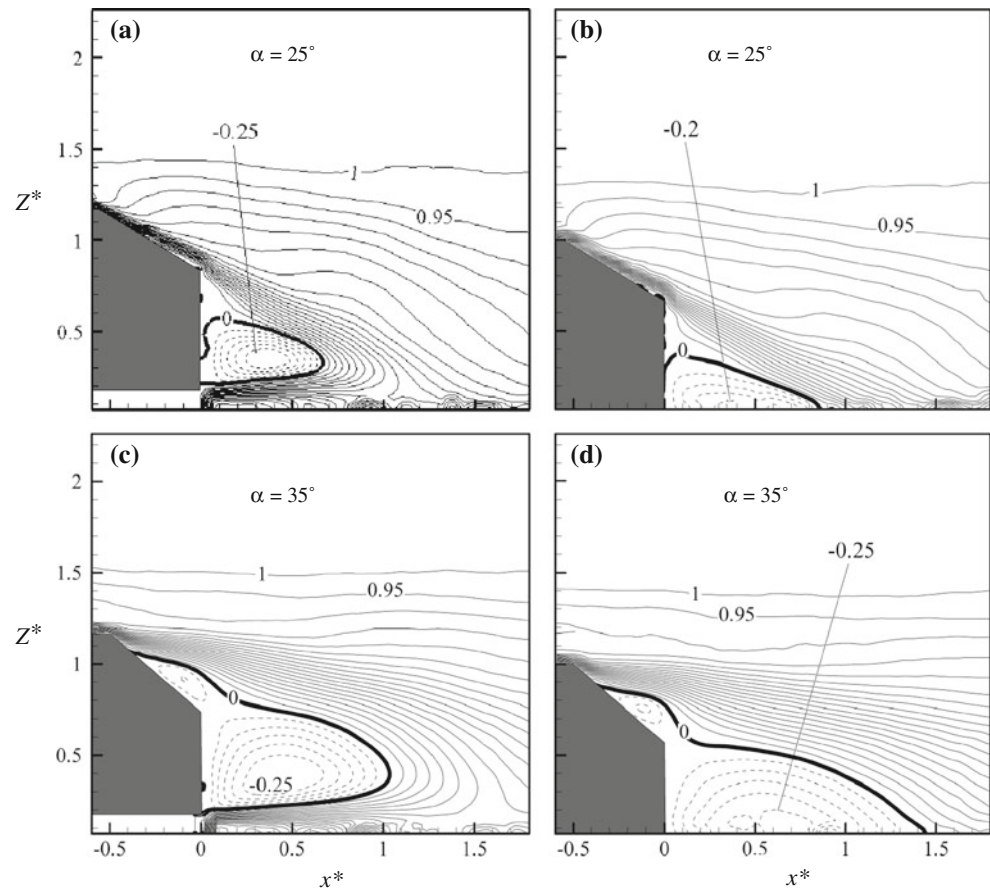
negative. This is expected since bubble "B" is largely associated with positive u and positive w (upwash), and bubble "A" is associated with positive u and negative w (downwash). The lower exceeds considerably the upper in the magnitude of $\overline{uw}^*$, well correlated with the maximum concentrations of bubbles "A" and "B". The concentration above the slant is due to the shear layer formed above the roof and is negative because positive u is mostly associated with negative w. Its magnitude is markedly weaker than the other two concentrations. At $\alpha = 35°$, the two negative concentrations merge into one because the recirculation over the slant is connected to that behind the base (Fig. 13c). At $g^* = 0$, there is no positive concentration behind the base because of the absence of bubble "B" (Fig. 13b, d), and the relatively high concentrations of the negative sign are well correlated with the high concentrations of the corresponding $\overline{\Omega}_y^*$-contours (Fig. 9b, d).

5 Transverse structures

The behaviors of the 3-D flow structure in the x–y plane are investigated by examining the transverse structures of vorticity. Figure 14 presents the typical Ω_z^*-contours in the x–y plane at $z^* = 0.59$ for $g^* = 0.174$ and $z^* = 0.50$ for $g^* = 0$, which are the mid-height of the model. As in the y–z and x–z planes, the instantaneous flow structure appears complicated. Consider first the case of $\alpha = 25°$. Two highly concentrated vorticity strips, emanating from the two side surfaces of the model, are located symmetrically about $y^* = 0$, viz. at $y^* \approx -0.7$ and 0.7, respectively, apparently corresponding to vortex "I" (Fig. 4a). Their maximum magnitudes of Ω_z^* reach 13 and 11, respectively, by far greater than their counterpart in the y–z plane (Figs. 4, 5). This is expected since the vorticity vector produced by the shear layer or the gradient of U in the y-direction is predominantly along the z-direction. The strip structures appear breaking down into patches at $x^* \approx 1.0$, probably as a result of interaction and merger with the C-pillar vortices. The patches are characterized by markedly lower maximum vorticity. It is noteworthy that the C-pillar vortex is downward inclined in the near wake, and hence, its induced vorticity concentrations in the x–y plane are of the same sign as those of vortex "I" on the same side. On another note, the oppositely signed structures tend to occur over $x^* = 0.35$–1.0 on the inner side ($y^* \approx \pm 0.5$) of the two strip structures, possibly resulting from interactions between the strip structures and
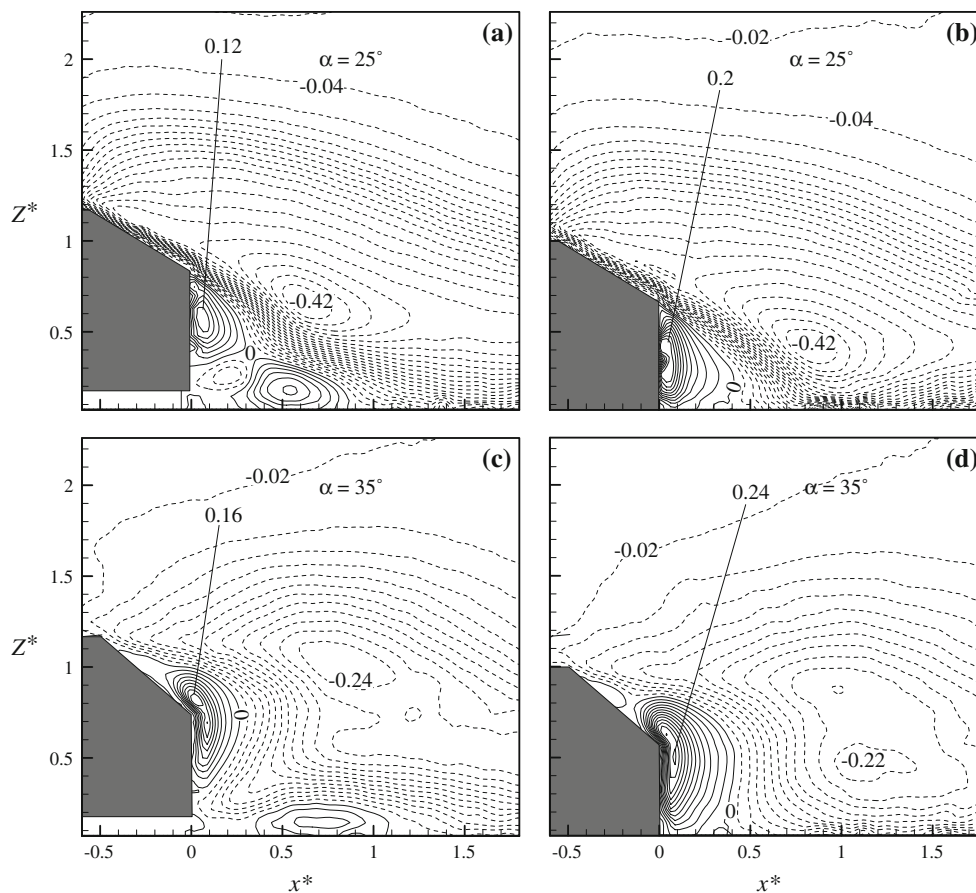
Fig. 12 Iso-contours of the averaged vertical velocity, $\overline{W}^*$, in the x–z plane at $y^* = 0$ ($Re_H = 5.26 \times 10^4$): (a, c) $g^* = 0.174$, **b, d** $g^* = 0$. The contour interval is 0.02

recirculatory bubbles "A" and "B". Furthermore, as observed in the y–z plane, a number of alternately signed structures are arranged in a row along the y-direction. Two such rows are discernible in Fig. 14a, as highlighted by thick broken lines. A quasi-longitudinal vortex, which is not oriented exactly longitudinally but inclined with respect to the x-axis, can show up in the x–y plane. Therefore, these structures are ascribed to the signatures of the alternately signed longitudinal structures associated with bubbles "A" or "B" observed in Figs. 4a and 5a. The association with "A" is more likely since the structures associated with "B" should be smaller, as will be discussed later in this section. The above flow features are also seen in the absence of clearance, i.e., $g^* = 0$ (Fig. 14b). The occurrence of the alternately signed structures, arranged in a row along the y-direction, at $g^* = 0$ where "bubble "B" does not exist, corroborates the assertion that the structures are associated with "A".

At $\alpha = 35°$, the flow structure, although appearing as complicated as at $\alpha = 25°$, exhibits considerable differences. Firstly, vorticity concentrations are more randomly distributed, all over the place at $g^* = 0.174$ (Fig. 14c), but

depleted in the recirculation region at $g^* = 0$ (Fig. 14d). At this configuration, flow separates from the upper edge of the slant, not the lower, and the absence of bubble "A" accounts for the more randomly distributed vorticity concentrations. At $g^* = 0$, bubble "B" does not exist either, and the vorticity concentrations separated from the upper edge of the slant can barely reach the recirculation region at $z^* = 0.5$. As such, there are few vorticity concentrations in this region. Secondly, the alternately signed concentrations, highlighted by thick broken lines, are still discernible at $g^* = 0.174$ but appear smaller-scaled, albeit slightly, than those at $\alpha = 25°$. The structures are connected to bubble "B", whose upwash motion should be surely enhanced in the absence of bubble "A". As a matter of fact, the hardly seen vorticity concentrations in the recirculation region at $g^* = 0$ (Fig. 14d) provide us with a support that the vorticity concentrations in the same area of Fig. 14c are connected to the occurrence of bubble "B". Bubble "B" is associated with smaller-scaled vorticity concentrations than "A". Please compare the longitudinal structures corresponding to bubble "A" with those to "B" (Fig. 5a). The difference in scale between the two bubbles
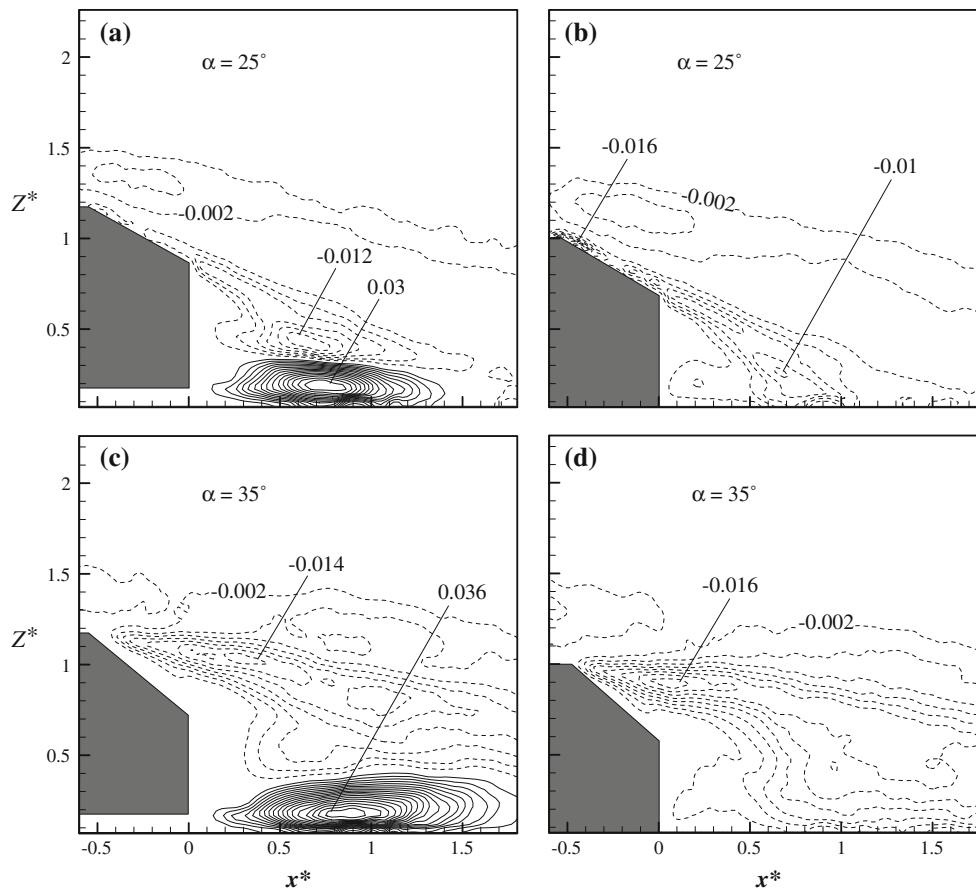
Fig. 13 Iso-contours of the $\overline{uw}^*$, in the x–z plane at $y^* = 0$ ($Re_H = 5.26 \times 10^4$): **a, c** $g^* = 0.174$, **b, d** $g^* = 0$. The contour interval is 0.002 and the cutoff level is ±0.002

is also evident in Ahmed et al.'s (1984) model (Fig. 1). We may therefore infer that the longitudinal structures associated with "A" should be larger in scale.

With the instantaneous transverse structures in mind, the corresponding mean vorticity field may be interpreted. In all cases, the iso-contours of $\overline{\Omega_z^*}$ in the x–y plane (Fig. 15) are approximately symmetrical about $y^* = 0$. At $\alpha = 25°$ and $g^* = 0.174$, three strip structures are seen on each side of $y^* = 0$ in the contours (Fig. 15a). The outer strip results largely from vortex "I" and its merging, starting from $x^* \approx 1.0$, with the C-pillar vortex. The middle oppositely signed strip may originate from the interaction between the C-pillar vortex and bubble "A", though the contributions from "I" could not be excluded. The sign of the inner strip is different from that of the middle strip, corroborating our proposition of bubble "A" in Fig. 6. There is a blank area between the two inner strips, which meet at about $x^* \approx 0.7$. Spanwise further away from the C-pillar vortex which induces an oppositely signed vorticity concentration (e.g., Fig. 5a), those vorticity concentrations in the row of alternately signed structures associated with "A" tend to occur more randomly along the spanwise direction,

enhancing the cancelation of each other. At $g^* = 0$ (Fig. 15b), a similar flow structure is observed, supporting the assertion that the middle and inner strips are linked with the occurrence of the bubble "A".

At $\alpha = 35°$, the outer strip only is observed in Fig. 15c, d. This is not unexpected since bubble "A" does not exist; furthermore, at $g^* = 0.174$, the alternately signed structures associated with "B", as seen in Fig. 14c, are located more randomly along the spanwise direction, promoting the cancelation of each other.

6 Summary and conclusions

The 3-D wake of the Ahmed model, with and without a clearance ($g^* = 0.174$) from wall, has been investigated at $Re_H = 5.26 \times 10^4$ in detail based on the PIV measurements in three orthogonal planes. Two distinct flow regimes are examined, as represented by the configurations of $\alpha = 25°$ and $35°$, respectively. The investigation leads to a number of findings, as summarized and incorporated in the schematic of the flow structure in Fig. 16.
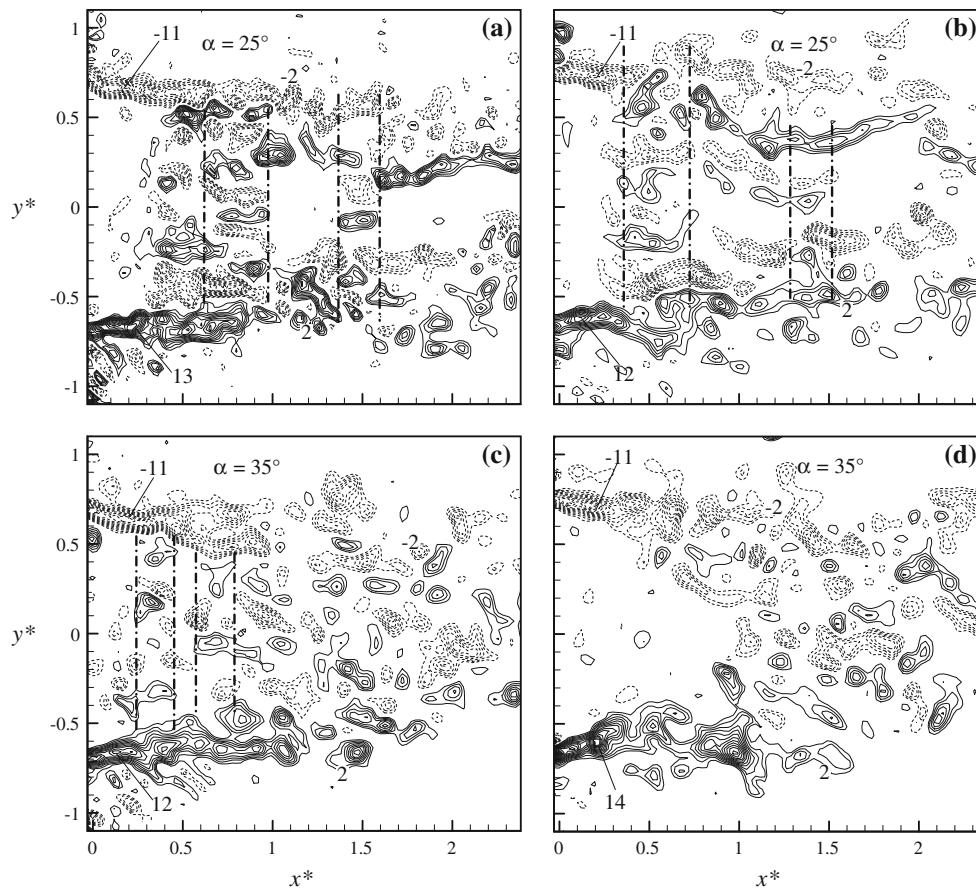
Fig. 14 Iso-contours of instantaneous transverse vorticity, Ω_z^*, in the x–y plane at $z^* = 0.59$ ($Re_H = 5.26 \times 10^4$): **a, c** $g^* = 0.174$ **b, d** $g^* = 0$. The contour interval is 1 and the cutoff level is ± 2

In the regime of $\alpha < 30°$, following modifications are made in Fig. 16a, compared with the classical model shown in Fig. 1:

1. Shear layer developed over the roof of the vehicle model flows largely along the slant under the effect of C-pillar vortex, but part of it tends to be diverted away from the slant, as suggested by the distributions of the Reynolds stresses (Fig. 13a).

2. While part of the shear layer separated from the slant is drawn into recirculation bubble "A", the other part forms a quasi-periodical wavy spanwise roll flowing over "A", as is suggested by instantaneous Ω_y-contours (Fig. 10a). The spectra of both fluctuating pressure and velocity signals measured on or behind the upper edge of the vertical base by Vino et al. (2005) displayed a pronounced peak at a dimensionless frequency of about 0.4 based on the square root of model frontal area. The result was also confirmed by our hotwire measurements, thus providing experimental evidence for quasi-periodical flow separation from the upper edge of the base. This spanwise roll produces alternately signed vorticity concentrations in the y–z plane (Figs. 4a, 5a) and in the x–y plane (Figs. 14a, 15a).

3. Separated from the lower edge of the base, the gap flow between the model underside and wall is partially drawn into recirculatory bubble "B" and partially rolls up, forming a spanwise roll that is separated quasi-periodically, again based on Vino et al.'s (2005) data. This roll is wrapped by longitudinal structures, as is supported by instantaneous longitudinal vorticity contours (Fig. 5a). Its signature in the x–y plane is also discernible by the alternately signed transverse vorticity concentrations in Fig. 14a.

4. Side vortex "I" is added, which is generated by the shear layer developed over the side surface. This vortex starts breaking down at $x^* \approx 1.0$ as a result of interaction and merger with the C-pillar vortex.

5. The previously observed lower vortex (Krajnovic and Davidson 2005a; Strachan et al. 2007) is added, which is generated by the pressure difference between flow inside the gap and that outside, in a manner similar to how the C-pillar vortices are generated.
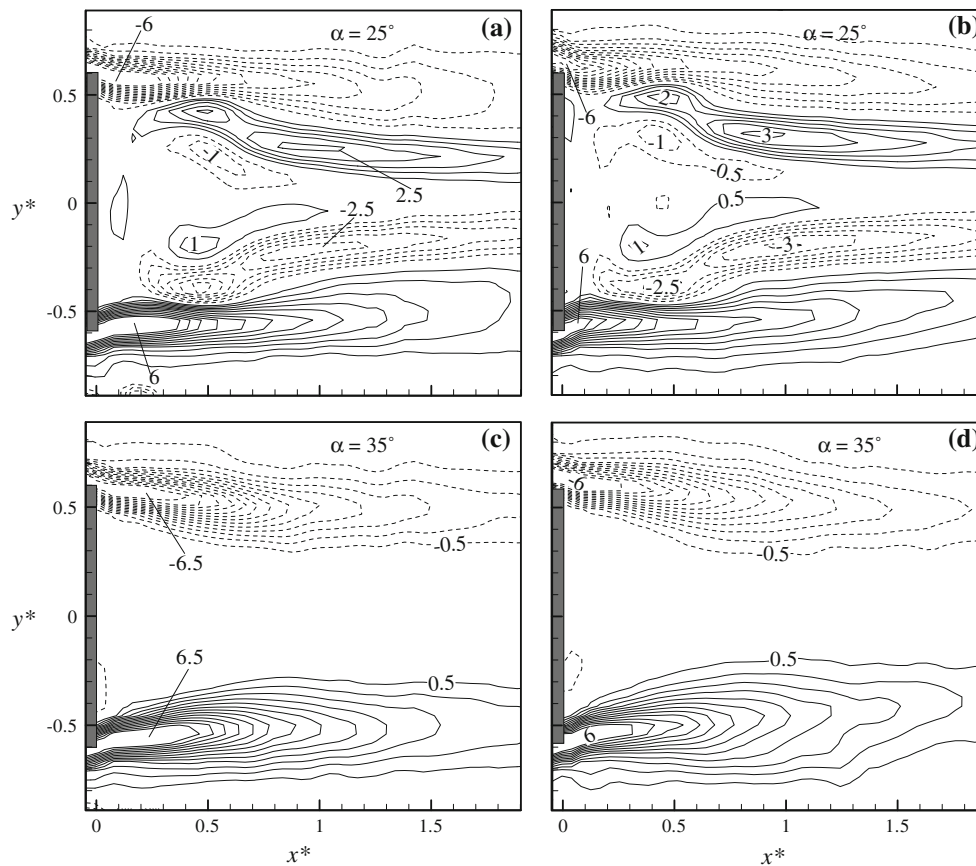
Fig. 15 Iso-contours of the averaged vertical component of vorticity, $\overline{\Omega}_z^*$, in the x–y plane at $z^* = 0.59$ ($Re_H = 5.26 \times 10^4$): **a, c** $g^* = 0.174$, **b, d** $g^* = 0$. The contour interval is 0.5 and the cutoff level is ± 0.5

6. One pair of gap vortices are included, which are generated by struts between the model underside and wall.

Previous studies indicated that flow separation on the slant surface at $\alpha = 25°$ is sensitive to Re_H and the sharpness of the edge between the roof and the slant surface. Whether the separation is present or not may have a strong influence on the flow topology around the Ahmed body (Sims-Williams 2001; Thacker et al. 2012). As such, it should be cautioned that the presently proposed flow structure model based on the measurements at a relatively low Re_H has yet to be validated for higher Re_H.

In the regime of $\alpha > 30°$, a flow structure model is presently proposed in Fig. 16b, complementing the rather simple model (e.g. Martinat et al. 2008), which was constructed based on Lienhardt et al.'s (2000) data, without many details of the flow structure. In the present model, the flow features 3 through 6 at $\alpha < 30°$ apply. Following changes are noted, as per the case of $\alpha < 30°$:

1. The shear layer developed over the top of the vehicle now separates near the upper edge of the slant (Figs. 9c, 10c, 11c, 12c and 13c) and is imbedded

with alternately signed longitudinal vortices, as evidenced in Figs. 4c and 5c.

2. The C-pillar vortex bursts, resulting in a greatly weakened strength, as is discernible in Figs. 4c.

3. Recirculation bubbles "E" over the slant and "A" behind the base merge into one (Figs. 9c, 10c, 11c, 12c and 13c).

A comparison is made between the wakes of the Ahmed model with and without a clearance. The extreme case at $g^* = 0$ eliminates the complication caused by the clearance, serving as an important reference for the understanding of the highly complicated vehicle wake. It is found that this clearance has a pronounced effect on the near wake of the vehicle model. Firstly, both bubbles "A" and "B" are altered in the absence of this clearance (Figs. 9b, d, 10b, d and 13), including the disappearance of bubble "B". Secondly, the recirculation region that is evident at $g^* \neq 0$ does not occur at $g^* = 0$, as indicated by the $\overline{U}^*$-contours (Fig. 11). Thirdly, the absence of the clearance changes the strengths of the C-pillar vortex "C" and side vortex "I" (Fig. 5).
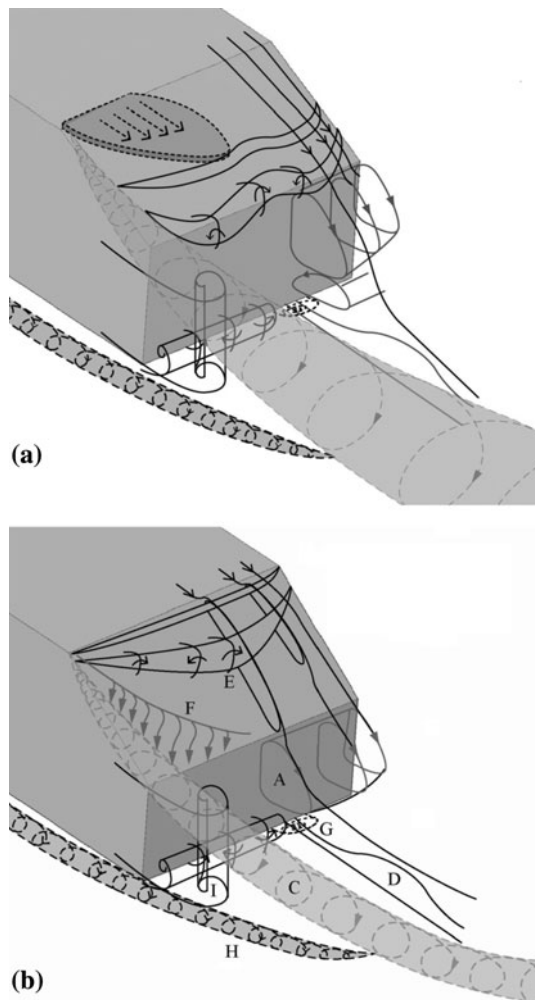
Fig. 16 Schematic of flow structure models: **a** $\alpha = 25°$, **b** $35°$

The mean velocity and the second moments of fluctuating velocities have been obtained in three orthogonal planes for different configurations, i.e., $g^* = 0.174$ and 0 and $\alpha = 25°$ and $35°$, which may be used for the validation of numerical models in the future.

Finally, it is worth commenting that the relative motion between the ground and the vehicle has a significant effect on the aerodynamics of road vehicles (e.g., Bearman et al. 1988; Hucho and Sovran 1993; Kim and Geropp 1998; Krajnovic and Davidson 2005c). Krajnovic and Davidson's (2005c) large eddy simulation of the Ahmed model of $\alpha = 25°$ ($Re_H = 2 \times 10^5$) showed that the floor motion resulted in the increased surface pressure on the rear slanted and vertical surfaces. Consequently, drag was reduced by 8 % and lift by 16 %. The floor motion further led to an enhanced periodicity of the flow. The effect on the flow over the rear slanted surface of the vehicle was also appreciable quantitatively, though not qualitatively. However, the flow behind the base seemed to be insensitive to

the floor motion, except the region close to the moving floor. It may be inferred that, although not considered presently, this effect should not invalidate the proposed models in Fig. 16.

References

Ahmed SR, Ramm G, Faltin G (1984) Some salient features of the time averaged ground vehicle wake. SAE Technical Paper No.: 840300, USA

Bearman PW (1997) Near wake flows behind two- and three-dimensional bluff bodies. J Wind Eng Ind Aerodyn 69–71:33–54

Bearman P W, De Beer D, Hamidy E & Harvey JK (1988) The effect of a moving floor on wind tunnel simulation of road vehicles, SAE-Paper 880245

Beaudoin JF, Aider JL (2008) Drag and lift reduction of a 3D bluff body using flaps. Exps. Fluids 44(4):491–501

Brunn A, Wassen E, Sperber D, Nitsche W, Thiele F (2007) "Active drag control for a generic car." In Active Flow Control (ed. King R), NNFM95, 247–259, Springer-Verlag Berlin Heidelberg

Farell C, Carrasquel S, Guben O, Patel VC (1977) Effect of wind tunnel walls on the flow past circular cylinders and cooling tower models. Journal Fluids Engineering 99:470–479

Huang JF, Zhou Y, Zhou TM (2006) Three-dimensional wake structure measurement using a modified PIV technique. Exp Fluids 40:884–896

Hucho WH, Sovran G (1993) Aerodynamics of Road Vehicles. Ann. Rev. Fluid Mech 25:485–537

Janssen LJ, Hucho WH 1974 Aerodynamische Formoptimierung der Type VW-Golf und VW-Sirocco. Kolloquium uber Inderstrie-aerodynamik, Achen, Part 3, 46–49

Joseph P, Amandolese X, Aider JL (2011) Drag reduction on the 25° slant angle Ahmed reference body using pulsed jets. Exps. Fluids: (Published online: 15/12/2011)

Kim MS, Geropp D (1998) Experimental investigation of the ground effect on the flow around some two-dimensional bluff bodies with moving-belt technique. J. Wind Eng. & Ind. Aero. 74–76:511–519

Krajnovic S, Davidson L (2002) Exploring the flow around a simplified bus with large eddy simulation and topological tools, in *The Serodynamics of Heavy Vehicles: Trucks, Buses and Trains*. Springer, Monterey, CA

Krajnovic S, Davidson L (2003) Numerical study of the flow around the bus-shaped body. ASME Journal of Fluids Engineering 125:500–509

Krajnovic S, Davidson L (2005a) Flow around a simplified car, Part 1: large eddy simulation. ASME Journal of Fluids Engineering 127:907–918

Krajnovic S, Davidson L (2005b) Flow around a simplified car, Part 2: understanding the flow. ASME Journal of Fluids Engineering 127:919–928

Krajnovic S, Davidson L (2005c) Influence of floor motions in wind tunnels on the aerodynamics of road vehicles. J Wind Eng Ind Aerodyn 93:677–696

Lienhart H, Becker S (2003) Flow and turbulence structures in the wake of a simplified car model. SAE Technical Paper No.: 2003-01-0656

Lienhardt H, Stoots C, Becker S (2000) Flow and turbulence structure in the wake of a simplified car model (Ahmed model). DGLR Fach symposium. der AG STAB, Stuttgart University

Martinat G, Bourguet R, Hoarau Y, dehaeze F, Jorez B, Braza M (2008) Numerical simulation of the flow in the wake of Ahmed body using detached eddy simulation and URANS modeling. In: Peng S-H, Haase W (eds) Adv. in Hybrid RANS-LES modeling, NNFM 97, Springer, Berlin, Heidelberg, pp 125–131

Minguez M, Pasquetti R, Serre E (2008) High-order large-eddy simulation of flow over the "Ahmed body" car model, Phys. Fluids 20, 095101 (17 pages)

Minguez M, Pasquetti R, Serre E (2009) Spectral vanishing viscosity stabilized LES of the Ahmed body turbulent wake. Communication in Computational Physics 5(2–4):635–648

Narasimha R, Prasad SN (1994) Leading edge shape for flat plate boundary layer studies. Exp Fluids 17:358–360

Oertel H (1990) Wakes behind blunt bodies. Annu Rev Fluid Mech 22:539–564

Sims-Williams DB (2001) Self-Excited Aerodynamic Unsteadiness Associated with Passenger Cars, PhD Thesis, University of Durham.

Sims-Williams DB, Duncan BD (2003) The Ahmed model unsteady wake: Experimental and computational analyses. SAE Technical Paper No.: 2003-01-1315.

Sims-Williams DB, Dominy RG, Howell JP (2001) An investigation into large scale unsteady structures in the wake of real and idealized hatchback car models. SAE Technical Paper No.: 2001-01-1041

Strachan RK, Knowles K, Lawson NJ (2007) The vortex structure behind an Ahmed reference model in the presence of a moving ground plane. Exp Fluids 42:659–669

Thacker A, Aubrun Leroy A, Devinant P (2012) Effect of suppressing the 3D separation on the rear slant on the flow structures around an Ahmed body. J Wind Eng Ind Aerodyn 107–108:237–243

Thompson M, Hourigan K, Sheridan J (1994) Three-dimensional instabilities in the cylinder wake, Int. Colloq. Jets, Wakes, Shear Layers, Melbourne, Australia, April 18-20, Paper 10

Vino G, Watkins S, Mousley P, Watmuff J, Prasad S (2005) Flow structures in the near-wake of the Ahmed model. Journal of Fluids and Structure 20:673–695

Wang HF, Zhou Y, Chan CK and Lam KS (2006) Effect of initial conditions on interaction between a boundary layer and a wall-mounted finite-length-cylinder wake. Physics of Fluids 18: Art. No. 065106

Williamson CHK (1996) Vortex dynamics in the cylinder wake. Ann. Rev. Fluid. Mech. 28:477

Wu J, Sheridan J, Welsh MC, Hourigan K (1996) Three-dimensional vortex structures in a cylinder wake. J Fluid Mech 312:201

Zhang H-Q, Fey U, Noack BR, König M, Eckelmann H (1995) On the transition of the cylinder wake. Phys Fluids 7:779

Zhang HJ, Zhou Y, Antonia RA (2000) Longitudinal and spanwise structures in a turbulent wake. Phys Fluids 12:2954–2964

Zhang HJ, Zhou Y, Whitelaw JH (2006) Near-field wing-tip vortices and exponential vortex solution. J. of Aircraft 43:446–449

Zhou Y, Antonia RA (1994) Critical points in a turbulent near wake. J Fluid Mech 275:59–81

Zhou Y, Yiu MW (2006) Flow structure, momentum and heat transport in a two-tandem-cylinder wake. J Fluid Mech 548:17–48